Rapid Communications

Measurement of transient strain induced by two-photon excitation

S. P. Zeuschner,[1,2] J.-E. Pudell,[1,2] A. von Reppert,[1] M. Deb,[1] E. Popova,[3] N. Keller,[3] M. Rössle,[2] M. Herzog,[1] and M. Bargheer[1,2,*]

[1]*Institute of Physics and Astronomy, University of Potsdam, Karl-Liebknecht-Str. 24-25, 14476 Potsdam, Germany*

[2]*Helmholtz-Zentrum Berlin für Materialien und Energie GmbH, Wilhelm-Conrad-Röntgen Campus, BESSY II, 12489 Berlin, Germany*

[3]*Groupe d'Etude de la Matiére Condensée (GEMaC), CNRS UMR 8635, Université Paris-Saclay, 78035 Versailles, France*

(Received 20 November 2019; accepted 17 March 2020; published 13 April 2020)

By ultrafast x-ray diffraction we quantify the strain from coherent and incoherent phonons generated by one- and two-photon absorption. We investigated the ferrimagnetic insulator bismuth-doped yttrium iron garnet, which is a workhorse for laser-induced spin dynamics that may be excited indirectly via phonons. We identify the two-photon absorption by the quadratic intensity dependence of the transient strain and confirm a short lifetime of the intermediate state via the inverse proportional dependence on the pump-pulse duration. We determine the two-photon absorption coefficient using the linear relation between strain and absorbed energy density. For large intensities of about 1 TW/cm^2 considerable strain amplitudes of 0.1% are driven exclusively by two-photon absorption.

DOI: 10.1103/PhysRevResearch.2.022013

Lattice dynamics is a unifying theme common to all laser-excited condensed matter systems, since their phonon subsystem provides a large bath for energy, entropy, and angular momentum transfer [1–4]. The ultrafast increase of the energy density in materials drives coherent atomic motion, i.e., sizable picosecond strain pulses [5–7], that add to the incoherent thermal expansion. Ultrafast x-ray diffraction (UXRD) has quantified these strain amplitudes generated in various materials, with a dependence on the incident fluence that is usually linear [5–8] or sublinear if saturation effects play a role [9]. In semiconductors and insulators the excitation of electrons across the band gap drives lattice strain [10–12]. However, the stresses by hot phonons often prevail [13]. In GaAs a nonlinear contribution to the fluence dependence of the strain adds to the saturating one-photon absorption [14]. Various time-resolved magneto-optical experiments in metallic magnets demonstrate the possibility to trigger and control magnetization precession [15–18], using laser-induced strain pulses. In contrast, most research on magnetic insulators, mainly oxides, emphasizes energy-efficient magnetization switching schemes [19,20] and nonthermal spin manipulation by the inverse Faraday effect [21], the inverse Cotton-Mouton effect [22], and photoinduced magnetic anisotropy [23]. Since these oxides have large band gaps, the processes are thought to proceed without absorption, and the generation of phonons is not always mentioned as a mechanism to drive spins. In some materials hybrid magnetoelastic modes are identified as the relevant excitations [24,25]. Among the magnetic oxides, yttrium iron garnet (YIG) provides the lowest magnon damping. Below the charge-transfer transitions identified with the band gap of YIG, there are weaker crystal-field *d*-*d* transitions down to about 800 nm [26,27]. A large magneto-optical contrast is achieved by bismuth substitution [28], which connects this workhorse of magnon spintronics [29,30] and spin caloritronics [31] to optomagnetism. Recent publications on ferrimagnetic garnets reported magnetization dynamics via thermally induced crystalline anisotropy modification [23,32,33], similar to previous work in antiferromagnets [34–36]. More specifically, optically excited coherent and incoherent phonons are reported to generate spin waves (SWs) [27,37,38]. A quadratic fluence dependence of the spin-wave amplitude was discovered in several garnets already with moderate fluences below 15 mJ/cm^2 [25,38].

Here, we present nondestructive UXRD measurements on the very same Bi:YIG film [38], to quantify the lattice dynamics upon below-band-gap femtosecond laser excitation with fluences up to 100 mJ/cm^2. This corresponds to intensities, which are typical of experiments that manipulate magnetization in insulators by femtosecond light pulses [19,33,37,38], and we find a pronounced quadratic fluence dependence of the strain amplitude that quantifies coherent and incoherent phonons as propagating strain pulses and localized thermal expansion, respectively. The strain amplitude is inversely proportional to the pump pulse duration, which indicates a short lifetime of the intermediate state during the two-photon excitation. This is a quantitative and direct structural measurement of transient strain generated dominantly by two-photon absorption. We contrast this two-photon absorption process with direct above-band-gap excitation using near-ultraviolet (NUV) pulses. In this case, the lattice strain η depends linearly on the excitation fluence.

We investigate two similar (100)-oriented thin films of 150 and 135 nm $Bi_xY_{3-x}Fe_5O_{12}$ (Bi:YIG) with $x = 1$ and 2, respectively, grown on a (100)-oriented $Gd_3Ga_5O_{12}$ (GGG) substrate, schematically pictured in Fig. 1(b). The single-crystalline films were grown by pulsed laser deposition.

*bargheer@uni-potsdam.de

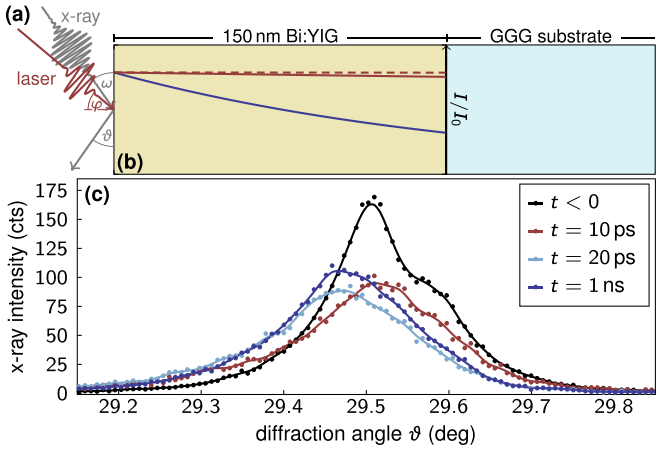

FIG. 1. (a) Sketched pump-probe geometry. (b) Sample structure and spatial intensity profiles in Bi:YIG for NUV (blue) and NIR illumination (red). For NIR light the linear absorption is negligible (dashed line) and it remains small (solid line) when including two-photon absorption, assuming an intensity of 1 TW/cm^2. (c) Scattered x-ray intensity is plotted as a function of ϑ, showing the (800) Bragg reflection of $Bi_2Y_1Fe_5O_{12}$ before 8 mJ/cm^2 NUV excitation and for a selection of pump-probe delays.

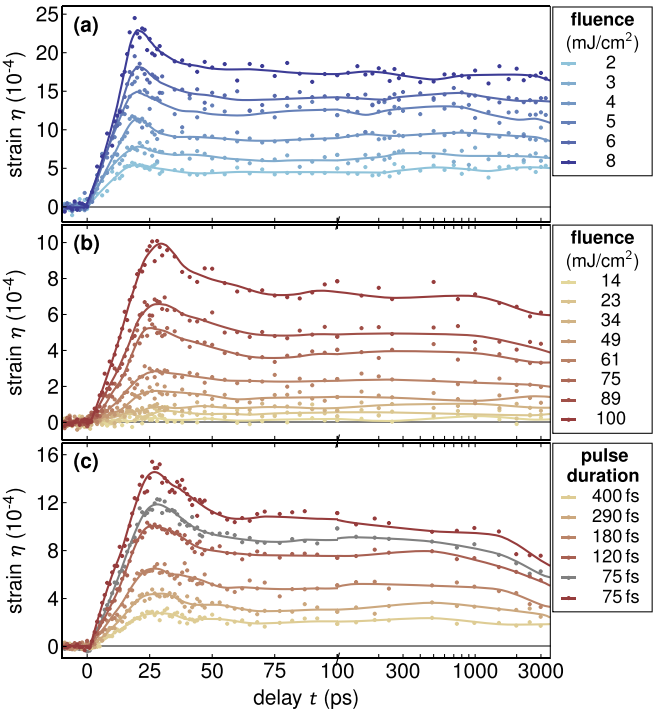

FIG. 2. Transient lattice strain η for different excitation parameters, measured with UXRD. Solid lines act as a guide to the eye. (a) Fluence series for $Bi_2Y_1Fe_5O_{12}$ with femtosecond NUV excitation. For $Bi_1Y_2Fe_5O_{12}$ we show (b) the fluence series with 120 fs NIR excitation and (c) the pulse duration series with 100 mJ/cm^2 NIR excitation. The gray data set has a similar pulse duration but opposite linear chirp.

X-ray diffraction and spectroscopic ellipsometry reveal similar structural and optical properties of both Bi:YIG samples. Although the bismuth substitution enhances the electronic d-d transition probabilities for photon energies just below the band-gap energy [39], the optical properties are essentially identical for both samples at the excitation wavelengths $\lambda_{NUV} = 400$ nm and $\lambda_{NIR} = 800$ nm of our experiments. This is verified by ellipsometry, which yields an optical penetration depth of 170 nm at λ_{NUV}. For λ_{NIR} ellipsometry only yields a lower bound for the penetration depth which is consistent with the literature value of 65 μm [26–28]. The intensity profiles for both excitation wavelengths are depicted true to scale in Fig. 1(b). For our experiments the relevant difference of the samples is the higher elastic constant for the lower bismuth concentration. The larger speed of sound is partially compensated by the increased layer thicknesses such that we qualitatively find the same transient response to laser excitation. The increased lattice constant upon doping [40] does not affect our results as we examine solely the relative changes of the lattice. Thus the two samples allow us to crosscheck the amplitudes and timings of the photoinduced strain transients.

The UXRD data, exemplarily depicted in Fig. 1(c), are measured at the laser-driven table-top plasma x-ray source (PXS) [41] at the University of Potsdam with a 200-fs x-ray pulse duration at a wavelength of 154 pm (Cu $K\alpha$). The samples are excited at a 1 kHz repetition rate by p-polarized NUV pulses at 400 nm or NIR pulses at 800 nm under an angle of $\varphi = 40^\circ$ [see Fig. 1(a)]. The incident fluence F_i is changed by a combination of a wave plate and polarizer. Changes in the spot size resulting from self-focusing at higher intensities, however, led us to adjust the full width at half maximum (FWHM) of the Gaussian-shaped pump pulses between 1.5 and 0.7 mm diameter, as controlled by a beam profiler. F_i is calculated by the top-hat approximation with the $1/e$ width for the laser excitation profile. The laser pulse duration is determined by a single-shot autocorrelator. X-ray pulses with a 0.3-mm-diam spot size probe the samples at delays up to $t = 3$ ns at a Bragg angle of $\omega = 29.5^\circ$ [see Fig. 1(a)], associated with the symmetric (800) reflection for both samples. In Fig. 1(c), the scattered x-ray intensity of Bi:YIG around $\omega = \vartheta$, detected with a Pilatus 100k area detector from Dectris, is exemplarily displayed for four different pump-probe delays after an 8 mJ/cm^2, NUV femtosecond excitation. The transient angular shift $\Delta\vartheta(t)$ of the Bragg reflection is calculated by the center-of-mass change of the scattered intensity before and after excitation [42]. From this, we calculate the mean transient out-of-plane strain (i.e., the relative change of the layer thickness) in the Bi:YIG layer, $\eta(t)$, via Bragg's law modified by a geometric scaling factor f. According to our diffraction geometry, with the sample and area detector at fixed diffraction angles, and for a convergent x-ray beam we use $f \approx 2$ [43,44],

$$\eta(t) = -f\,\Delta\vartheta(t)\cot(\omega). \tag{1}$$

First, we investigated the transient strain of Bi:YIG as a function of the excitation fluence for NUV illumination to determine the response to an above-band-gap excitation. The results for $Bi_2Y_1Fe_5O_{12}$ are shown in Fig. 2(a) and yield the typical linear scaling of the strain amplitude with the fluence in accordance with other studies on semiconductors and insulators [12,45]. This dependence is analyzed by the blue linear fit in Fig. 3(a), where the average strain $\overline{\eta}$ in

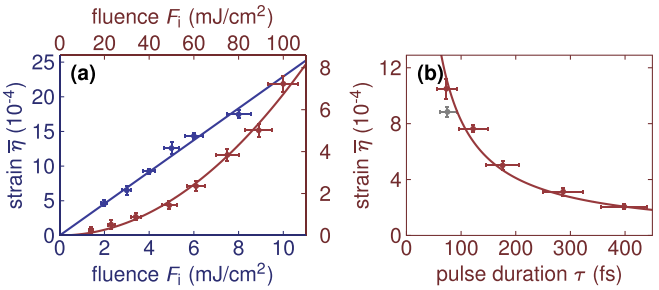

FIG. 3. Averaged lattice strain $\overline{\eta}$ in Bi:YIG between 75 ps and 1 ns evaluated from the data set in Fig. 2. (a) $\overline{\eta}$ as a function of the fluence at NUV excitation of $Bi_2Y_1Fe_5O_{12}$ (blue) and NIR excitation of $Bi_1Y_2Fe_5O_{12}$ (red). The NUV data are fitted with a linear function and a quadratic fluence dependence is observed for the NIR excitation as predicted by the presented modeling [see Eq. (7)]. (b) Pulse duration dependence of $\overline{\eta}$ upon NIR excitation of $Bi_1Y_2Fe_5O_{12}$. The gray data point was obtained under different chirp conditions. The solid line results from Eq. (7) with the same parameters as in (a). The vertical error bars are the standard deviation of η and the horizontal error bars are estimated from the pump spot size fluctuation and the GDD of the mirrors.

Bi:YIG from 75 ps to 1 ns is displayed as a function of the NUV fluence. The transient strain data in Fig. 2 exhibit multiple features characteristic of coherent and incoherent phonons. During the first 50 ps, the rising edge, the local maximum at 25 ps, and the falling edge are associated with a coherent and bipolar phonon wave packet launched by the absorption of an ultrashort laser pulse [12]. The time to reach the maximum expansion/strain is governed by the sound velocity in Bi:YIG and the film thickness. The falling edge relates to the movement of the expansive part of the bipolar wave packet out of the Bi:YIG layer [12]. The exact temporal behavior of the measured average strain depends on the spatial form of the wave packet [12]. The strain beyond 50 ps arises from heating, which is proportional to the absorbed energy [1,46,47]. Within our measurement window of 3 ns the thermal expansion shows almost no relaxation because of the slow heat transport out of Bi:YIG, as expected from the low thermal conductivity of garnet [48,49]. The dynamics of the film with $x = 1$ is identical when we scale the timing according to the different sound velocity and thickness.

Following the experiments for the excitation of spin waves [24,25,38,50], we excited Bi:YIG with NIR light with a short pulse duration (150 fs) and incident fluences up to 100 mJ/cm^2. We used the very same $x = 1$ sample as Deb *et al.* [38]. At fluences comparable to the NUV excitation no significant strain was detected. The results for fluences larger than 10 mJ/cm^2 are displayed in Fig. 2(b) and show a quadratic dependence of $\eta(t)$ on the fluence. Substantiated by the red line in Fig. 3(a), this quadratic fluence dependence indicates a two-photon strain generation process. Although the transient strain response for NIR excitation shown in Figs. 2(b) and 2(c) is very similar to the above-band-gap excitation shown in Fig. 2(a), three small differences in the observed strain signatures require discussion. The maximum at 25 ps in Fig. 2(b) is slightly delayed, because the higher sound velocity $v_1 = 6.3$ nm/ps for $x = 1$ as compared to $v_2 = 5.4$ nm/ps for $x = 2$ [40,51] is overcompensated by the layer thickness d. Second, the subsequent falling edge shows an almost linear strain decrease from 25 to 50 ps for NIR excitation, whereas for NUV excitation the slope shows an exponential-like decrease. This is observed for both samples and is due to the nearly homogeneous nonlinear absorption in contrast to the steeper intensity profile for linear absorption, displayed in Fig. 1(b). The absorption profiles lead to different stress profiles inside the layer. Consequently, a rectangular-shaped bipolar strain wave is launched upon NIR excitation and a semiexponential-shaped bipolar strain wave is launched upon NUV excitation [8]. The average strain in the Bi:YIG layer is shaped accordingly [52], which we monitor directly with UXRD [3,8,53]. The different intensity profiles also determine the deposition of heat. This explains the third difference observed at timescales beyond 1 ns when $\eta(t)$ retains a constant value for NUV excitation and decreases at NIR excitation. We attribute this to a stronger heat gradient at the Bi:YIG/GGG interface and faster cooling to the substrate for NIR excitation.

We conclude our measurements with a variation of the NIR pulse duration to examine the lifetime of the transient state of the two-photon process. At a fluence of 100 mJ/cm^2 we tuned the pump pulse duration from $\tau = 75$ to 400 fs. The transient strain response, depicted in Fig. 2(c), is qualitatively very similar to the data in Fig. 2(b). The dependence of the average strain $\overline{\eta}(\tau)$ on the pulse duration τ is analyzed in Fig. 3(b). The fit shows an inverse proportionality between $\overline{\eta}$ and τ. The two-photon absorption for the shortest pulse durations of 75 fs with opposite linear chirp show deviations which we attribute to a higher-order chirp. The fit in Fig. 3(b) only includes the red data points which have the same sign of the linear chirp which was controlled by the grating compressor of the laser system. We corrected the pulse durations measured at the autocorrelator according to the group delay dispersion GDD $\approx -500 \pm 200$ fs^2 of the mirrors between the autocorrelator and the sample.

Both the fluence and pulse duration dependence of the strain are consistent with a model which is based on one- and two-photon absorption processes. In the following we present the modeling to fit the strain data in Fig. 3 and to determine the two-photon absorption coefficient β of Bi:YIG for NIR light. Lambert-Beer's law can be modified by a second-order term to account for two-photon absorption [see Eq. (2)] [54,55]. Starting from the attenuation of light in matter at the depth z due to one- and two-photon absorption, we solve the following equation for the intensity I,

$$\frac{\partial I}{\partial z} = -\alpha I - \beta I^2, \tag{2}$$

where α is the one- and β the two-photon absorption coefficient. In the case of linear one-photon absorption, i.e., for NUV light, we set $\beta = 0$, which results in Lambert-Beer's law [see Eq. (3)]. In the case of NIR light, we set $\alpha = 0$ to model the strain generated solely by two-photon absorption as suggested by the data in Fig. 3(a). If I_0 is the incident intensity on the Bi:YIG layer, the solutions of Eq. (2) are

$$I(z) = \begin{cases} I_0 e^{-\alpha z} & \text{for NUV,} \\ \frac{I_0}{1+\beta I_0 z} & \text{for NIR.} \end{cases} \tag{3}$$

Since the layer thickness is much smaller than the penetration depth of the NIR light, we may Taylor-expand Eq. (3) at $z = 0$, i.e., $I(z) = I_0 - \beta I_0^2 z + O(z^2)$. The linear spatial intensity dependence is a good approximation for NIR light [see Fig. 1(b)]. For time-resolved measurements, the incident intensity I_0 is time dependent. In this experiment, the excitation pulse can be well approximated by a Gaussian envelope $I_0(t) = 2\sqrt{\ln 2/\pi}\, F_\mathrm{i}/\tau \exp(-4\ln 2\, t^2/\tau^2)$, where F_i is the incident fluence, and τ is the pulse duration at FWHM. The absorbed fluence inside the Bi:YIG layer $F_\mathrm{a}(F_\mathrm{i}, \tau)$ is calculated via temporal integration of the intensity difference from the sample surface ($z = 0$) to the layer-substrate interface ($z = d$)

$$F_\mathrm{a}(F_\mathrm{i}, \tau) = \int_{-\infty}^{\infty} I_0(t) - I(z = d, t)dt \tag{4}$$

$$= \begin{cases} (1 - e^{-\alpha d})F_\mathrm{i} & \text{for NUV,} \\ \sqrt{\frac{\ln 4}{\pi}}\beta d \frac{F_\mathrm{i}^2}{\tau} - O\left(\frac{F_\mathrm{i}^3}{\tau^2}\right) & \text{for NIR.} \end{cases} \tag{5}$$

The stress σ on the lattice resulting from the energy density deposited by the pump pulse $\rho^\mathrm{Q} = F_\mathrm{a}/d$ is given by the macroscopic Grüneisen parameter Γ via $\sigma = \Gamma\rho^\mathrm{Q}$ [3,46,47,56]. In the one-dimensional (1D) geometry of a homogeneously excited thin film with a cubic symmetry aligned to the sample surface, the strain response perpendicular to the surface is given by $\eta = \sigma/C_{11}$, where C_{11} is the cubic elastic constant. We estimate the mean strain in the Bi:YIG layer via the linear NUV absorption ($\beta = 0$),

$$\overline{\eta}_\mathrm{NUV} = \frac{\Gamma}{C_{11}d}(1 - e^{-\alpha d})F_\mathrm{i}. \tag{6}$$

The 2.1×10^{-4} per mJ/cm^2 calculated from Eq. (6) is in reasonable agreement with the strain $\overline{\eta}_\mathrm{NUV} = 2.3 \times 10^{-4}$ per mJ/cm^2 extracted from the blue line in Fig. 3(a). Here, we used a film thickness of $d = 135$ nm, the linear absorption coefficient for NUV light $\alpha = 6 \times 10^4$ cm^{-1}, the elastic constant $C_{11} = 190$ GPa for $Bi_2Y_1Fe_5O_{12}$, and the Grüneisen parameter of YIG, $\Gamma \approx 1$, reported in the literature [26,40,51,57]. The lattice strain $\overline{\eta}$ generated via nonlinear NIR absorption can also be calculated in the same manner with a different value of $C_{11} = 230$ GPa for $Bi_1Y_2Fe_5O_{12}$,

$$\overline{\eta}_\mathrm{NIR} = \frac{\Gamma}{C_{11}}\sqrt{\frac{\ln 4}{\pi}}\beta\frac{F_\mathrm{i}^2}{\tau}. \tag{7}$$

This equation describes the functional dependence of the strain on the fluence F_i and the pulse duration τ which we discovered experimentally upon NIR excitation. The red curves in Fig. 3 are calculated with Eq. (7), fitting the data precisely if we use $\beta = 2.4$ cm/GW as the two-photon absorption coefficient. We visualized the spatial intensity profile according to two-photon absorption in Fig. 1(b) by the red solid line. As a crosscheck we note that $\alpha I < \beta I^2$, already for comparably low intensities of $I = 0.1$ TW/cm^2 if we use the literature value $\alpha = 150$ cm^{-1} for NIR light [26]. This justifies neglecting the linear absorption term during the evaluation of the NIR data, since βI^2 is orders of magnitude larger than αI at intensities higher than $I = 1$ TW/cm^2.

A two-photon absorption coefficient of $\beta_\mathrm{YIG} = 130$ cm/GW was reported for undoped YIG at photon energies of $(1.17 + 1.93)$ eV $= 3.1$ eV [58]. Mainly, a two-step process via the ${}^6A_{1g}({}^6S) \rightarrow {}^4T_{1g}({}^4G)$ and subsequent ${}^4T_{1g}({}^4G) \rightarrow {}^4T_{1g}({}^4P)$ Fe^{3+}-ion transitions in YIG and Bi:YIG accounts for the two-photon absorption in both materials [27,59,60], i.e., the two-photon transition proceeds via real and short-lived levels. The bismuth substitution affects the electronic and optical properties of YIG, e.g., increasing spin-orbit coupling, absorption, and even second-harmonic generation (SHG) efficiency [39,61,62]. In particular, the very weak ${}^6A_{1g}({}^6S) \rightarrow {}^4T_{1g}({}^4G)$ transition energy shifts with doping and therefore modulates the one- and two-photon absorption coefficients. According to our modeling the previously reported β_YIG would yield a strain of 4% and an absorption of 60% at large peak intensities of 1 TW/cm^2, which contradicts the measured values of 0.1% strain and less than 5% absorption.

To summarize, we used UXRD to directly measure the strain in nanolayered Bi:YIG excited via one- and two-photon absorption. We identify the two-photon process by the quadratic fluence dependence and the inversely proportional pulse duration dependence of the photoexcited strain. The latter also proves that the intermediate state is short lived. We substantiate our findings by a quantitative fit with Lambert-Beer's law with a two-photon absorption extension in combination with the Grüneisen approach, where the absorbed energy is proportional to the lattice strain, independent of how the photon energy is absorbed. From this, we determine the two-photon absorption coefficient $\beta \approx 2$ cm/GW for exciting $Bi_1Y_2Fe_5O_{12}$ at 800 nm. We believe that our quantitative evaluation of the strain generated by two-photon absorption is particularly important for a full understanding of light-driven spin manipulation in magnetic insulators [23,27,32–38], but it has more general relevance for ultrafast science on supposedly nonabsorbing or transparent matter. The large peak intensities around 1 TW/cm^2 necessary to drive 0.1% strain can be achieved both by high pump fluences and short pulse durations.

We acknowledge the BMBF for the financial support via 05K16IPA and the DFG via BA 2281/8-1 and BA 2281/11-1. M.D. thanks the Alexander von Humboldt Foundation for financial support. We acknowledge the precharacterization of the crystalline thin films at the XPP-KMC3 synchrotron-radiation beamline D13.2 at the BESSY II electron storage ring operated by the Helmholtz-Zentrum Berlin.

[1] J. Pudell, A. A. Maznev, M. Herzog, M. Kronseder, C. H. Back, G. Malinowski, A. von Reppert, and M. Bargheer, Layer specific observation of slow thermal equilibration in ultrathin metallic nanostructures by femtosecond X-ray diffraction, Nat. Commun. **9**, 3335 (2018).

[2] M. Highland, B. C. Gundrum, Y. K. Koh, R. S. Averback, D. G. Cahill, V. C. Elarde, J. J. Coleman, D. A. Walko, and E. C. Landahl, Ballistic-phonon heat conduction at the nanoscale as revealed by time-resolved x-ray diffraction and time-domain thermoreflectance, Phys. Rev. B **76**, 075337 (2007).

[3] J. Pudell, A. von Reppert, D. Schick, F. Zamponi, M. Rössle, M. Herzog, H. Zabel, and M. Bargheer, Ultrafast negative thermal expansion driven by spin disorder, Phys. Rev. B **99**, 094304 (2019).

[4] C. Dornes, Y. Acremann, M. Savoini, M. Kubli, M. J. Neugebauer, E. Abreu, L. Huber, G. Lantz, C. A. F. Vaz, H. Lemke, E. M. Bothschafter, M. Porer, V. Esposito, L. Rettig, M. Buzzi, A. Alberca, Y. W. Windsor, P. Beaud, U. Staub, D. Zhu *et al.*, The ultrafast Einstein–de Haas effect, Nature (London) **565**, 209 (2019).

[5] C. Thomsen, H. T. Grahn, H. J. Maris, and J. Tauc, Surface generation and detection of phonons by picosecond light pulses, Phys. Rev. B **34**, 4129 (1986).

[6] P. Ruello and V. E. Gusev, Physical mechanisms of coherent acoustic phonons generation by ultrafast laser action, Ultrasonics **56**, 21 (2015).

[7] O. Matsuda, M. C. Larciprete, R. Li Voti, and O. B. Wright, Fundamentals of picosecond laser ultrasonics, Ultrasonics **56**, 3 (2015).

[8] D. Schick, M. Herzog, A. Bojahr, W. Leitenberger, A. Hertwig, R. Shayduk, and M. Bargheer, Ultrafast lattice response of photoexcited thin films studied by X-ray diffraction, Struct. Dyn. **1**, 064501 (2014).

[9] D. Daranciang, M. J. Highland, H. Wen, S. M. Young, N. C. Brandt, H. Y. Hwang, M. Vattilana, M. Nicoul, F. Quirin, J. Goodfellow, T. Qi, I. Grinberg, D. M. Fritz, M. Cammarata, D. Zhu, H. T. Lemke, D. A. Walko, E. M. Dufresne, Y. Li, J. Larsson *et al.*, Ultrafast Photovoltaic Response in Ferroelectric Nanolayers, Phys. Rev. Lett. **108**, 087601 (2012).

[10] C. Rose-Petruck, R. Jimenez, T. Guo, A. Cavalieri, C. W. Siders, F. Rksi, J. A. Squier, B. C. Walker, K. R. Wilson, and C. P. J. Barty, Picosecond-milliangstrom lattice dynamics measured by ultrafast X-ray diffraction, Nature (London) **398**, 310 (1999).

[11] K. Sokolowski-Tinten, C. Blome, C. Dietrich, A. Tarasevitch, M. Horn von Hoegen, D. von der Linde, A. Cavalleri, J. Squier, and M. Kammler, Femtosecond X-Ray Measurement of Ultrafast Melting and Large Acoustic Transients, Phys. Rev. Lett. **87**, 225701 (2001).

[12] D. Schick, M. Herzog, H. Wen, P. Chen, C. Adamo, P. Gaal, D. G. Schlom, P. G. Evans, Y. Li, and M. Bargheer, Localized Excited Charge Carriers Generate Ultrafast Inhomogeneous Strain in the Multiferroic $BiFeO_3$, Phys. Rev. Lett. **112**, 097602 (2014).

[13] M. Bargheer, N. Zhavoronkov, J. C. Woo, D. S. Kim, M. Woerner, and T. Elsaesser, Excitation mechanisms of coherent phonons unravelled by femtosecond X-ray diffraction, Phys. Status Solidi A **243**, 2389 (2006).

[14] G. J. Williams, S. Lee, D. A. Walko, M. A. Watson, W. Jo, D. R. Lee, and E. C. Landahl, Direct measurements of multi-photon induced nonlinear lattice dynamics in semiconductors via time-resolved x-ray scattering, Sci. Rep. **6**, 39506 (2016).

[15] J. V. Jäger, A. V. Scherbakov, T. L. Linnik, D. R. Yakovlev, M. Wang, P. Wadley, V. Holy, S. A. Cavill, A. V. Akimov, A. W. Rushforth, and M. Bayer, Picosecond inverse magnetostriction in galfenol thin films, Appl. Phys. Lett. **103**, 032409 (2013).

[16] J.-W. Kim, M. Vomir, and J.-Y. Bigot, Ultrafast Magnetoacoustics in Nickel Films, Phys. Rev. Lett. **109**, 166601 (2012).

[17] J.-W. Kim, M. Vomir, and J.-Y. Bigot, Controlling the spins angular momentum in ferromagnets with sequences of picosecond acoustic pulses, Sci. Rep. **5**, 8511 (2015).

[18] D. Afanasiev, I. Razdolski, K. M. Skibinsky, D. Bolotin, S. V. Yagupov, M. B. Strugatsky, A. Kirilyuk, T. Rasing, and A. V. Kimel, Laser Excitation of Lattice-Driven Anharmonic Magnetization Dynamics in Dielectric $FeBO_3$, Phys. Rev. Lett. **112**, 147403 (2014).

[19] A. Stupakiewicz, K. Szerenos, D. Afanasiev, A. Kirilyuk, and A. V. Kimel, Ultrafast nonthermal photo-magnetic recording in a transparent medium, Nature (London) **542**, 71 (2017).

[20] F. Hansteen, A. Kimel, A. Kirilyuk, and T. Rasing, Femtosecond Photomagnetic Switching of Spins in Ferrimagnetic Garnet Films, Phys. Rev. Lett. **95**, 047402 (2005).

[21] A. V. Kimel, A. Kirilyuk, P. A. Usachev, R. V. Pisarev, A. M. Balbashov, and T. Rasing, Ultrafast non-thermal control of magnetization by instantaneous photomagnetic pulses, Nature (London) **435**, 655 (2005).

[22] C. Tzschaschel, K. Otani, R. Iida, T. Shimura, H. Ueda, S. Günther, M. Fiebig, and T. Satoh, Ultrafast optical excitation of coherent magnons in antiferromagnetic NiO, Phys. Rev. B **95**, 174407 (2017).

[23] A. Stupakiewicz, A. Maziewski, I. Davidenko, and V. Zablotskii, Light-induced magnetic anisotropy in Co-doped garnet films, Phys. Rev. B **64**, 064405 (2001).

[24] Y. Hashimoto, S. Daimon, R. Iguchi, Y. Oikawa, K. Shen, K. Sato, D. Bossini, Y. Tabuchi, T. Satoh, B. Hillebrands, G. E. W. Bauer, T. H. Johansen, A. Kirilyuk, T. Rasing, and E. Saitoh, All-optical observation and reconstruction of spin wave dispersion, Nat. Commun. **8**, 15859 (2017).

[25] Y. Hashimoto, D. Bossini, T. H. Johansen, E. Saitoh, A. Kirilyuk, and T. Rasing, Frequency and wavenumber selective excitation of spin waves through coherent energy transfer from elastic waves, Phys. Rev. B **97**, 140404(R) (2018).

[26] G. B. Scott, D. E. Lacklison, and J. L. Page, Absorption spectra of $Y_3Fe_5O_{12}$ (YIG) and $Y_3Ga_5O_{12}$:Fe^{3+}, Phys. Rev. B **10**, 971 (1974).

[27] M. Deb, P. Molho, B. Barbara, and J.-Y. Bigot, Controlling laser-induced magnetization reversal dynamics in a rare-earth iron garnet across the magnetization compensation point, Phys. Rev. B **97**, 134419 (2018).

[28] J. M. Robertson, S. Wittekoek, T. J. A. Popma, and P. F. Bongers, Preparation and optical properties of single crystal thin films of bismuth substituted iron garnets for magneto-optic applications, Appl. Phys. **2**, 219 (1973).

[29] A. V. Chumak, V. Vasyuchka, A. Serga, and B. Hillebrands, Magnon spintronics, Nat. Phys. **11**, 453 (2015).

[30] A. A. Serga, A. V. Chumak, B. Hillebrands, A. A. Serga, B. Hillebrands, A. V. Chumak, and T. Neumann, YIG magnonics, J. Phys. D **43**, 264002 (2010).

[31] G. E. W. Bauer, E. Saitoh, and B. J. van Wees, Spin caloritronics, Nat. Mater. **11**, 391 (2012).

[32] L. A. Shelukhin, V. V. Pavlov, P. A. Usachev, P. Y. Shamray, R. V. Pisarev, and A. M. Kalashnikova, Ultrafast laser-induced changes of the magnetic anisotropy in a low-symmetry iron garnet film, Phys. Rev. B **97**, 014422 (2018).

[33] C. S. Davies, K. H. Prabhakara, M. D. Davydova, K. A. Zvezdin, T. B. Shapaeva, S. Wang, A. K. Zvezdin, A. Kirilyuk, T. Rasing, and A. V. Kimel, Anomalously Damped

Heat-Assisted Route for Precessional Magnetization Reversal in an Iron Garnet, Phys. Rev. Lett. **122**, 027202 (2019).

[34] A. V. Kimel, A. Kirilyuk, A. Tsvetkov, R. V. Pisarev, and T. Rasing, Laser-induced ultrafast spin reorientation in the antiferromagnet $TmFeO_3$, Nature (London) **429**, 850 (2004).

[35] A. M. Kalashnikova, A. V. Kimel, R. V. Pisarev, V. N. Gridnev, A. Kirilyuk, and T. Rasing, Impulsive Generation of Coherent Magnons by Linearly Polarized Light in the Easy-Plane Antiferromagnet $FeBO_3$, Phys. Rev. Lett. **99**, 167205 (2007).

[36] A. M. Kalashnikova, A. V. Kimel, R. V. Pisarev, V. N. Gridnev, P. A. Usachev, A. Kirilyuk, and T. Rasing, Impulsive excitation of coherent magnons and phonons by subpicosecond laser pulses in the weak ferromagnet $FeBO_3$, Phys. Rev. B **78**, 104301 (2008).

[37] B. Koene, M. Deb, E. Popova, N. Keller, T. Rasing, and A. Kirilyuk, Spectrally resolved optical probing of laser induced magnetization dynamics in bismuth iron garnet, J. Phys.: Condens. Matter **28**, 276002 (2016).

[38] M. Deb, E. Popova, M. Hehn, N. Keller, S. Petit-Watelot, M. Bargheer, S. Mangin, and G. Malinowski, Femtosecond Laser-Excitation-Driven High Frequency Standing Spin Waves in Nanoscale Dielectric Thin Films of Iron Garnets, Phys. Rev. Lett. **123**, 027202 (2019).

[39] M. Deb, E. Popova, A. Fouchet, and N. Keller, Magneto-optical Faraday spectroscopy of completely bismuth-substituted $Bi_3Fe_5O_{12}$ garnet thin films, J. Phys. D **45**, 455001 (2012).

[40] G. G. Siu, C. M. Lee, and Y. Liu, Magnons and acoustic phonons in $Y_{3-x}Bi_xFe_5O_{12}$, Phys. Rev. B **64**, 094421 (2001).

[41] D. Schick, A. Bojahr, M. Herzog, C. Von Korff Schmising, R. Shayduk, W. Leitenberger, P. Gaal, and M. Bargheer, Normalization schemes for ultrafast x-ray diffraction using a table-top laser-driven plasma source, Rev. Sci. Instrum. **83**, 025104 (2012).

[42] The double-peak structure of the unexcited sample results from the $K\alpha_1$ and $K\alpha_2$ photons emitted by the source. The inhomogeneous excitation results in a broadening of the maxima.

[43] D. Schick, R. Shayduk, A. Bojahr, M. Herzog, C. von Korff Schmising, P. Gaal, and M. Bargheer, Ultrafast reciprocal-space mapping with a convergent beam, J. Appl. Crystallogr. **46**, 1372 (2013).

[44] M. Kozina, T. Hu, J. S. Wittenberg, E. Szilagyi, M. Trigo, T. A. Miller, C. Uher, A. Damodaran, L. Martin, A. Mehta, J. Corbett, J. Safranek, D. A. Reis, and A. M. Lindenberg, Measurement of transient atomic displacements in thin films with picosecond and femtometer resolution, Struct. Dyn. **1**, 034301 (2014).

[45] H. Wen, P. Chen, M. P. Cosgriff, D. A. Walko, J. H. Lee, C. Adamo, R. D. Schaller, J. F. Ihlefeld, E. M. Dufresne, D. G. Schlom, P. G. Evans, J. W. Freeland, and Y. Li, Electronic Origin of Ultrafast Photoinduced Strain in $BiFeO_3$, Phys. Rev. Lett. **110**, 037601 (2013).

[46] A. von Reppert, J. Pudell, A. Koc, M. Reinhardt, W. Leitenberger, K. Dumesnil, F. Zamponi, and M. Bargheer, Persistent nonequilibrium dynamics of the thermal energies in the spin and phonon systems of an antiferromagnet, Struct. Dyn. **3**, 054302 (2016).

[47] T. Henighan, M. Trigo, S. Bonetti, P. Granitzka, D. Higley, Z. Chen, M. P. Jiang, R. Kukreja, A. Gray, A. H. Reid, E. Jal, M. C. Hoffmann, M. Kozina, S. Song, M. Chollet, D. Zhu, P. F. Xu, J. Jeong, K. Carva, P. Maldonado *et al.*, Generation mechanism of terahertz coherent acoustic phonons in Fe, Phys. Rev. B **93**, 220301(R) (2016).

[48] N. P. Padture and P. G. Klemens, Low thermal conductivity in garnets, J. Am. Ceram. Soc. **80**, 1018 (2005).

[49] G. A. Slack and D. W. Oliver, Thermal conductivity of garnets and phonon scattering by rare-earth ions, Phys. Rev. B **4**, 592 (1971).

[50] I. Razdolski, A. Alekhin, N. Ilin, J. P. Meyburg, V. Roddatis, D. Diesing, U. Bovensiepen, and A. Melnikov, Nanoscale interface confinement of ultrafast spin transfer torque driving non-uniform spin dynamics, Nat. Commun. **8**, 15007 (2017).

[51] M. Deb, E. Popova, M. Hehn, N. Keller, S. Mangin, and G. Malinowski, Picosecond acoustic-excitation-driven ultrafast magnetization dynamics in dielectric Bi-substituted yttrium iron garnet, Phys. Rev. B **98**, 174407 (2018).

[52] D. Schick, P. Gaal, A. Bojahr, W. Leitenberger, R. Shayduk, A. Hertwig, I. Vrejoiu, M. Herzog, and M. Bargheer, Ultrafast x-ray diffraction studies of photoexcited coherent phonons in $SrRuO_3$ thin films, arXiv:1301.3324.

[53] S. P. Zeuschner, T. Parpiiev, T. Pezeril, A. Hillion, K. Dumesnil, A. Anane, J. Pudell, L. Willig, M. Rössle, M. Herzog, A. von Reppert, and M. Bargheer, Tracking picosecond strain pulses in heterostructures that exhibit giant magnetostriction, Struct. Dyn. **6**, 24302 (2019).

[54] M. Bass, E. W. van Stryland, D. R. Williams, and W. L. Wolfe, *Handbook of Optics Volume I*, 2nd ed. (McGraw-Hill, New York, 1995).

[55] J.-C. Diels and W. Rudolph, *Ultrashort Laser Pulse Phenomena: Fundamentals, Techniques, and Applications on a Femtosecond Time Scale*, 2nd ed. (Elsevier/Academic, Amsterdam, 2006), p. 652.

[56] A. Koc, M. Reinhardt, A. von Reppert, M. Rössle, W. Leitenberger, M. Gleich, M. Weinelt, F. Zamponi, and M. Bargheer, Grueneisen-approach for the experimental determination of transient spin and phonon energies from ultrafast x-ray diffraction data: Gadolinium, J. Phys.: Condens. Matter **29**, 264001 (2017).

[57] G. A. Saunders, S. C. Parker, N. Benbattouche, and H. L. Alberts, Elastic and nonlinear acoustic properties of the terbium iron garnet $Tb_3Fe_5O_{12}$ in relation to those of other garnets, Phys. Rev. B **46**, 8756 (1992).

[58] S. I. Shablaev and R. V. Pisarev, Two-photon absorption spectroscopy of electronic states in yttrium iron garnet $Y_3Fe_5O_{12}$, J. Magn. Soc. Jpn. **11**, 19 (1987).

[59] J. F. Dillon, Optical absorptions and rotations in the ferrimagnetic garnets, J. Phys. Radium **20**, 374 (1959).

[60] K. A. Wickersheim and R. A. Lefever, Absorption spectra of ferric iron-containing oxides, J. Chem. Phys. **36**, 844 (1962).

[61] T. Oikawa, S. Suzuki, and K. Nakao, First-principles study of spin-orbit interactions in bismuth iron garnet, J. Phys. Soc. Jpn. **74**, 401 (2005).

[62] G. Petrocelli, S. Martellucci, and M. Richetta, Bismuth induced enhancement of the second-harmonic generation efficiency in bismuth-substituted yttrium iron garnet films, Appl. Phys. Lett. **63**, 3402 (1993).